THE JOURNAL OF PHYSICAL CHEMISTRY Letters

Cite This: J. Phys. Chem. Lett. 2018, 9, 3604−3611

Letter

pubs.acs.org/JPCL

# Electronic Properties of Free-Standing Surfactant-Capped Lead Halide Perovskite Nanocrystals Isolated in Vacuo

Aleksandar R. Milosavljević,*[,†] Dušan K. Božanić,[†,‡] Subha Sadhu,[§,#] Nenad Vukmirović,[∥] Radovan Dojčilović,[‡,▽] Pitambar Sapkota,[§,⊥] Weixin Huang,[§] John Bozek,[†] Christophe Nicolas,[†] Laurent Nahon,[†] and Sylwia Ptasinska[§,⊥]

[†]Synchrotron SOLEIL, l'Orme des Merisiers, Saint Aubin, BP48, 91192 Gif sur Yvette Cedex, France

[‡]Vinča Institute of Nuclear Sciences, University of Belgrade, P.O. Box 522, 11001 Belgrade, Serbia

[§]Radiation Laboratory, University of Notre Dame, Notre Dame, Indiana 46556, United States

[∥]Scientific Computing Laboratory, Center for the Study of Complex Systems, Institute of Physics Belgrade, University of Belgrade, Pregrevica 118, 11080 Belgrade, Serbia

[⊥]Department of Physics, University of Notre Dame, Notre Dame, Indiana 46556, United States

Supporting Information

**ABSTRACT:** We report an investigation of lead halide perovskite $CH_3NH_3PbBr_3$ nanocrystals and associated ligand molecules by combining several different state-of-the-art experimental techniques, including synchrotron radiation-based XPS and VUV PES of free-standing nanocrystals isolated in vacuum. By using this novel approach for perovskite materials, we could directly obtain complete band alignment to vacuum of both $CH_3NH_3PbBr_3$ nanocrystals and the ligands widely used in their preparation. We discuss the possible influence of the ligand molecules to apparent perovskite properties, and we compare the electronic properties of nanocrystals to those of bulk material. The experimental results were supported by DFT calculations.

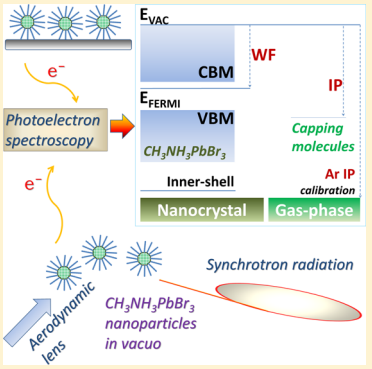


Lead halide perovskites (LHPs) have been attracting enormous attention in recent years as low-cost and unprecedentedly efficient absorbers for solar cells.[1−7] Very recently, LHP nanocrystals (NCs) have gained in interest due to advantages over the polycrystalline LHP thin films in several critical aspects, for example, the optical transitions are less affected by structural defects, and they exhibit higher stability against degradation, unique optical versatility, and high photoluminescence and thus offer new prospects in optoelectronic applications including solar cells, light-emitting diodes, photodetectors, and memory devices.[8−10] Further research is still required to achieve the characteristics necessary for their commercial exploitation.[8−10] In particular, accurate and precise determination of the electronic structure of any specific material under study is a fundamentally important step that provides necessary information for developing applications.[11,12] Determination of the complete band structure still appears to be a challenging task for many materials, most notably obtaining precise values of the vacuum level ($E_{vac}$), work function (WF), valence band maximum (VBM), and conduction band minimum (CBM).[11,13,14] Matter in the NC form adds an additional level of complexity due to the drastically increased importance of surface properties over the bulk, size confinement effects and possible influence of ligand molecules in the case of ligand-assisted reprecipitation (LARP)[10] production.

This Letter reports a novel approach for studying the electronic properties of LHP NCs by performing laboratory-based X-ray photoelectron spectroscopy (XPS), as well as synchrotron-based XPS, VUV photoelectron spectroscopy (PES), and photoelectron−photoion coincidence spectroscopy (PEPICO) on isolated NCs, produced by atomization of NC organocolloids transported and focused into the vacuum of the spectrometer by an aerodynamic lens.[15−17] We investigated NCs of methylammonium lead bromide ($CH_3NH_3PbBr_3$, $MAPbBr_3$), which represents one of the most investigated LHPs (see refs 11, 13, and 18−20 and references therein) and has been attracting significant attention as a candidate as an absorber material for solar cells.[8−10,21−26] A complete determination of the electronic structure was obtained experimentally by combining photoemission measurements of isolated NCs at the SOLEIL synchrotron (France), hereafter denoted gas-phase XPS, and of the same NCs deposited on a substrate (Notre Dame Radiation Laboratory, USA), hereafter

**Received:** May 9, 2018
**Accepted:** June 14, 2018
**Published:** June 14, 2018






DOI: 10.1021/acs.jpclett.8b01466
J. Phys. Chem. Lett. 2018, 9, 3604−3611

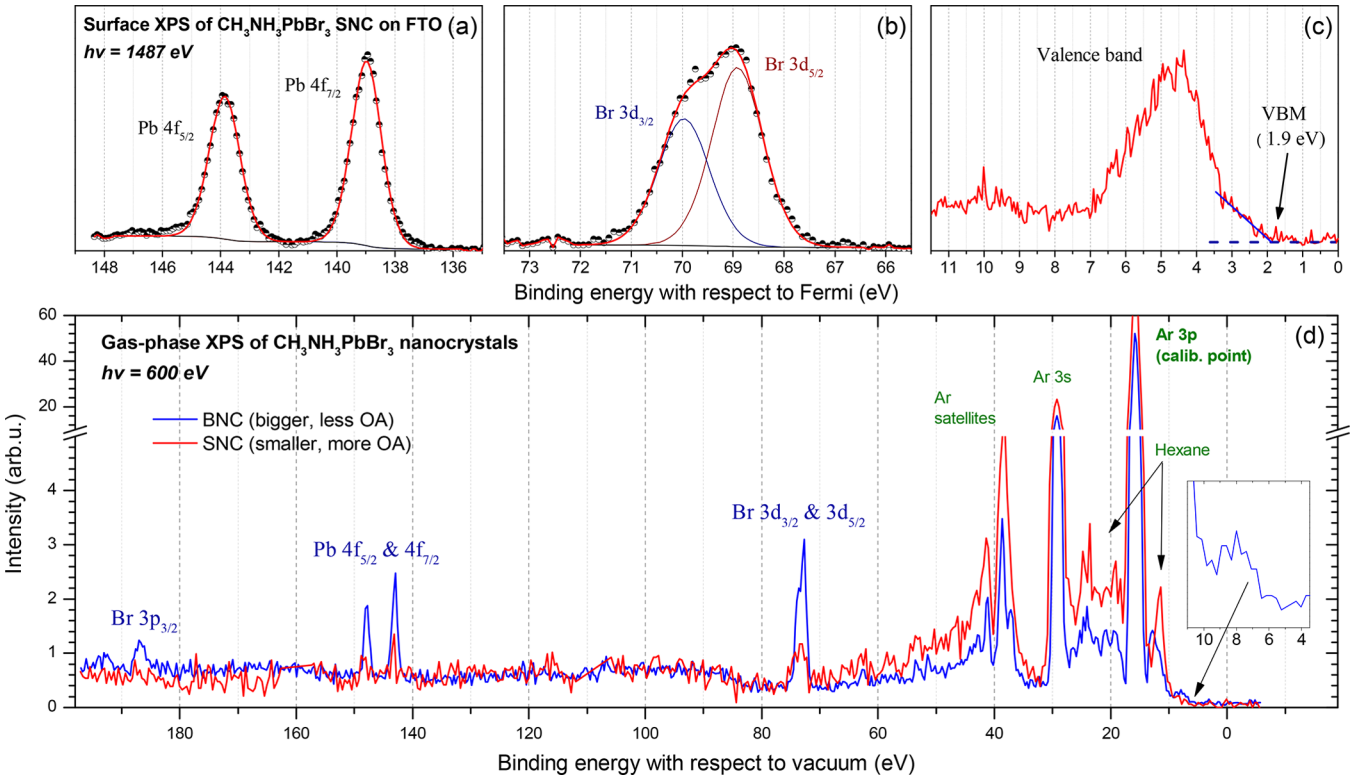


**Figure 1.** (a–c) Surface XPS of deposited $MAPbBr_3$ NCs of 11 ± 3 nm on a FTO surface recorded using a SPECS Surface Nano Analysis GmbH apparatus (photon energy of 1486.7 eV). (d) Gas-phase XPS of isolated $MAPbBr_3$ NCs of 11 ± 3 nm (SNC, red line) and 20 ± 5 nm (BNC, blue line), recorded at the SOLEIL synchrotron facility, at a photon energy of 600 eV.

denoted surface XPS. The experimental results are compared with calculations based on density functional theory (DFT). Furthermore, we have performed the first detailed study of the electronic properties of the attached ligand molecules used to terminate the crystal growth, based on both gas-phase XPS and VUV PEPICO measurements, also compared with DFT calculation results.

$MAPbBr_3$ NCs dispersed in hexane were prepared according to the emulsion method reported previously[27] that employs methylammonium bromide ($CH_3NH_3Br$) and lead bromide ($PbBr_2$) as precursors dissolved in dimethylformamide (DMF), as well as octylamine (OL) and oleic acid (OA) as phase transfer/capping agents (see the Experimental and Theoretical Section and Figure SI1 in the Supporting Information for a detailed description). The size of the resulting NCs was investigated by transmission electron microscopy and found to be in the range of 11 ± 3 nm (Figure SI2), hereafter denoted as small NCs (SNCs). The perovskite crystal structure was verified by X-ray diffraction analysis (XRD) (Figure SI3). The XRD pattern obtained is consistent with that of previously published reports exhibiting the characteristic diffraction pattern of the cubic $MAPbBr_3$ crystal structure.[28] An optical band gap ($E_g$) of 2.34 eV (530 nm) (Figure SI4) was observed by UV–vis absorption spectroscopy, in accordance with a previously reported value for NCs.[22]

LHP NCs were deposited on a fluorine-doped tin oxide (FTO) substrate to obtain the standard high-energy surface XPS spectra given in Figure 1a–c. These spectra reveal the binding energies of the Pb and Br core levels, as well as the VBM, relative to the Fermi level (BEF) calibrated according to the adventitious carbon (see the Experimental and Theoretical Section). The binding energies obtained (BEFs) are Pb $4f_{7/2}$ = 139.0 ± 0.5 eV, Pb $4f_{5/2}$ = 143.9 ± 0.5 eV; Br $3d_{5/2}$ = 68.9 ± 0.5 eV, Br $3d_{3/2}$ = 69.9 ± 0.5 eV; and VBM = 1.9 ± 0.5 eV. Pb and Br values are in a very good agreement with those previously reported for the $MAPbBr_3$ NCs and microcrystals (Pb $4f_{7/2}$ = 139.0 eV; $4f_{5/2}$ = 143.9 eV)[22] and thin films (Pb $4f_{7/2}$ = 139.1 eV).[18] On the other hand, the VBM for $MAPbBr_3$ NCs was reported previously at 2.46 eV,[22] which is significantly higher than the present value of 1.9 eV (Figure 1c). The previous[22] value was obtained in the standard way, as a linear extrapolation of the whole valence band edge obtained from XPS experiment. Applying the same method with the present measurement would give a VBM even above 2.5 eV. As has been already suggested and discussed previously, this procedure overestimates the real VBM.[11,29]

Gas-phase XPS measurements of isolated $MAPbBr_3$ NCs were performed using a recently developed nanoparticle injection technique,[15] with important modifications, both in the setup and the sample preparation, due to the specific characteristics of the LHP material (see the Experimental and Theoretical Section). We also prepared NCs, denoted BNC, using a smaller amount of the OA. The resulting colloid contained larger nanoparticles with a diameter of about 20 nm for which the size confinement will be less pronounced. The reported electronic properties of the BNCs should therefore correspond to that of the bulk material $MAPbBr_3$. Figure 1d presents a gas-phase XPS result obtained at a photon energy of 600 eV for both types of NCs. The 3p, 3s, and satellite peaks of Ar, which was used as a carrier gas for the NCs, is clearly seen between 15 and 60 eV binding energy (BE). Features from the solvent hexane molecules, some of which pass through from the atomizer to the XPS spectrometer, are also visible in this



DOI: 10.1021/acs.jpclett.8b01466
J. Phys. Chem. Lett. 2018, 9, 3604–3611

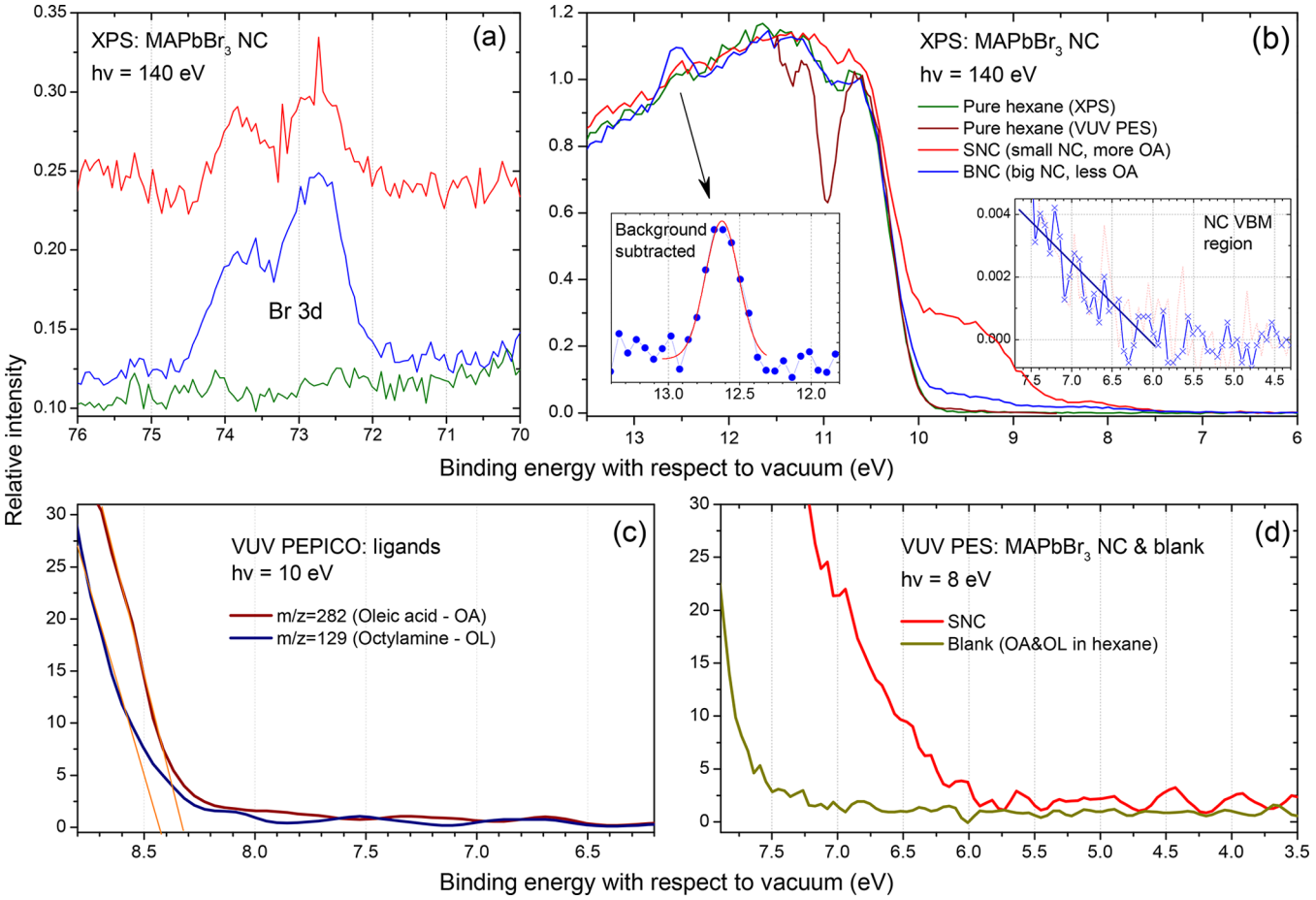


**Figure 2.** (a,b) Gas-phase XPS of isolated $MAPbBr_3$ NCs of 11 ± 3 nm (SNC, red line) and 20 ± 5 nm (BNC, blue line), as well as pure hexane solution (green line) recorded at the PLEIADES beamline at a photon energy of 140 eV. The dark red line in (b) represents the VUV PEPICO spectrum of the pure hexane solution recorded at the DESIRS beamline. The insets in (b) show a zoom-in of the regions of interest. (c) VUV PEPICO spectra for selected fragments of the OA and OL from the SNC solution, recorded at a photon energy of 10 eV. (d) VUV PES of isolated $MAPbBr_3$ NCs of 11 ± 3 nm (red line) and "blank solution" containing only OA and OL (olive line) recorded at a photon energy of 8 eV.

region. Finally, the peaks corresponding to the ionization of Br 3d, 3p, and Pb 4f core levels from the LHP NCs are clearly resolved at Br $3p_{3/2}$ = 186.72 ± 0.20 eV, Pb $4f_{7/2}$ = 143.06 ± 0.20, Pb $4f_{5/2}$ = 147.91 ± 0.20 eV; Br $3d_{3/2}$ = 73.85 ± 0.20 eV, Br $3d_{5/2}$ = 72.76 ± 0.20 eV; and VBM ≈ 6 eV. The signal from the LHP NCs is clearly much stronger for BNC due to the significantly lower surface coverage of the organic ligands, which influences the escape depth of photoelectrons even for relatively high kinetic energy electrons. There is no apparent shift between SNC and BNC Br and Pb core levels.

Because the aerodynamic lens used to inject the nanoparticles into the spectrometer focuses the NCs to a narrow beam in the interaction region while the gaseous components are diffusely injected into the spectrometer, this XPS method allows us to distinguish photoelectrons coming from either the gas phase or the NC beam (see Figure SI5). All detected species, the NCs (containing $MAPbBr_3$ and ligands OA and OL), hexane, and argon are isolated in vacuum and are not in physical or electrical contact with anything in the spectrometer. The kinetic energies and corresponding binding energies of the measured photoelectrons are therefore referenced to the vacuum level. The BE with respect to vacuum (BEV) scale was calibrated according to the ionization potential (IP) of Ar $3p_{3/2}$ (see the Experimental and Theoretical Section).

Isolated NCs in the gas phase still possess an intrinsic work function.[14,17,30] An accurate experimental determination of the work function of a semiconductor material is not a trivial task.[14] Commonly used methods such as Kelvin probe and low-energy electron cutoff from PES or the recently introduced gas-phase PES using a near-ambient XPS[14] may be even less accurate for NCs deposited on a substrate. For NCs isolated in the gas phase, on the other hand, one cannot calibrate the position of the Fermi level. In the present work, the work function is determined by combining the surface-deposited and gas-phase free-standing NC XPS measurements (Figure 1) using the Pb 4f core level: WF = BEV(Pb $4f_{7/2}$) − BEF(Pb $4f_{7/2}$) = (4.1 ± 0.5) eV. This work function for $MAPbBr_3$ NCs of about 11 nm diameter appears to be very close to that recently reported for bulk $MAPbBr_3$ film, extracted from a combined experimental (PES) and theoretical study.[11] Our value was determined experimentally from the core-level BE of the central Pb atom and with an accuracy simply determined by the uncertainty of the measured electron kinetic energies (dominantly) and the reference IPs of Ar gas and the adventitious carbon (in the present case).

The NCs of MAPbBr used in this study were inevitably covered by organic ligand molecules (OA and OL). To further investigate the effects of the ligands on the obtained results, the surface properties of $MAPbBr_3$ NCs were enhanced by



DOI: 10.1021/acs.jpclett.8b01466
J. Phys. Chem. Lett. 2018, 9, 3604−3611

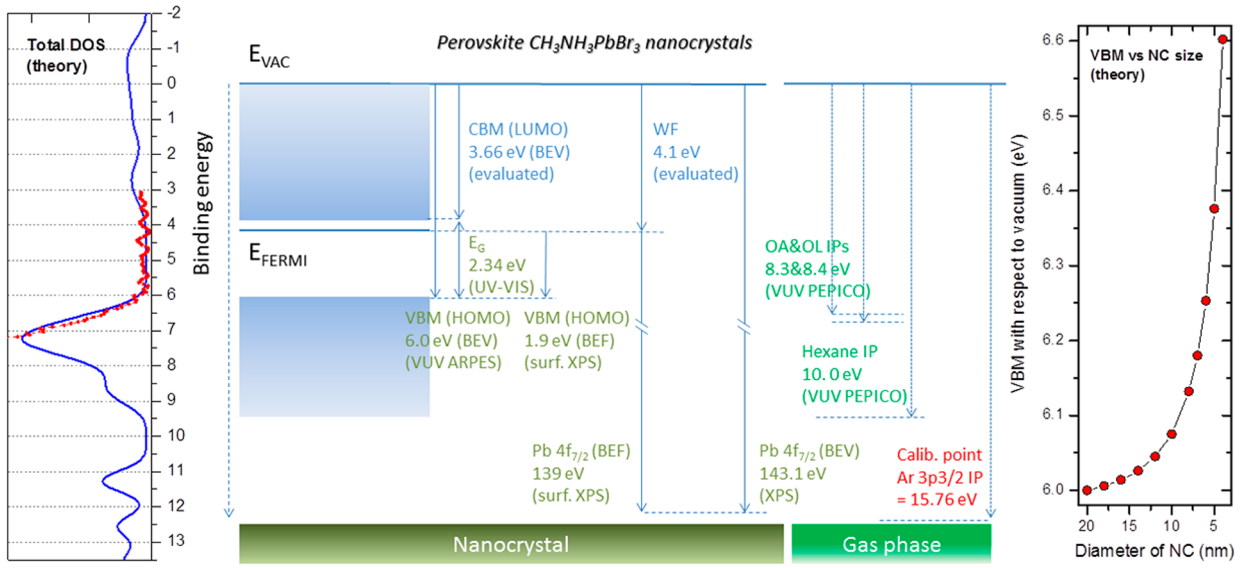


**Figure 3.** Left panel: Calculated DOS for $MAPbBr_3$ cubic perovskite bulk material, broadened by a Gaussian with a standard deviation of 0.3 eV (blue curve) and normalized VUV PES of isolated $MAPbBr_3$ NCs of 11 ± 3 nm (red circles). Middle panel: Experimentally obtained band alignment of $MAPbBr_3$ NCs of 11 ± 3 nm (SNC). Directly measured values are presented in olive, while evaluated values (from these measurements) are presented in blue. Measured IPs for single molecules are in green. Right panel: Calculated quantum confinement energy in the valence band of $MAPbBr_3$ cubic perovskite NCs as a function of their diameter.

performing gas-phase XPS using a lower photon energy of 140 eV, providing both higher energy resolution and lower kinetic energy photoelectrons with very short inelastic mean free paths, below 1 nm.[13] A wide-BE range gas-phase XPS spectrum of NCs and pure hexane solution is presented in Figure SI6, with segments of interest shown in Figure 2a,b. The smaller SNCs, with greater ligand coverage relative to the large BNC particles, clearly exhibit an increased background and reduced Br 3d signal, but with no apparent shift of 3d core levels (Figure 2a). The valence band region (Figure 2b) is also seen to be strongly affected by the presence of ligands. The feature observed at a BE of 12.6 eV (inset in Figure 2b) is ascribed to mixed C and N p-type orbitals from the methylammonium cation of $MAPbBr_3$ NCs with the aid of the calculations (see Figure SI11). The ligand valence signal clearly comes from the nanoparticles (NC beam), in contrast to the hexane valence band, as can be seen from the gas-phase XPS spectrum shown in Figure SI7. The valence band edges for the two NC samples, SNC and BNC, are difficult to define precisely from the present gas-phase XPS spectra as they are strongly masked by signal from the ligands covering the surface. Still, close inspection of the region at 4.5−7.5 eV reveals a threshold at about 6 eV both for SNC and BNC (right inset in Figure 2b). The perfect agreement of the hexane valence band from gas-phase XPS and VUV PES data recorded independently on different beamlines and just calibrated to the same Ar IP (Figure 2b) constitutes a convincing cross-check of the consistency of the data acquired with the two methods.

With VUV photoemission, the low kinetic energies of the photoelectrons result in electron scattering lengths that are comparable to or even greater than the size of the NCs; therefore, the whole volume of the particles can be probed. VUV PEPICO measurements using a photon energy of 10 eV (mass spectrum given in Figure SI8) allowed precise determination of the IPs for OL and OA (Figure 2c), 8.40 ± 0.05 and 8.30 ± 0.05 eV, respectively. This is in reasonably good agreement with the DFT calculations that give 8.02 eV for OL and 8.01 eV for OA. The DFT calculated value for the IP of hexane of 9.6 eV was also lower than the measured one of 10 eV. The difference between calculated and experimental values might originate from the fact that the calculation assumes ideally straight molecule in vacuum, while the exact shape of the molecule is not well-known and it is partially surrounded by other ligand molecules and the nanoparticle. One should also note that the accuracy of the B3LYP functional in predicting the IP of organic molecules is typically 0.2−0.3 eV (see Table 1 in ref 31), being therefore comparable to the difference between our theoretical and experimental results.

Having determined the IPs of isolated OA and OL molecules to above 8.3 eV, we performed VUV angle-resolved photoemission spectroscopy (ARPES) of the $MAPbBr_3$ aerosol below this energy at 8 eV photon energy to obtain the precise experimental value of the $MAPbBr_3$ NC VBM, avoiding any influence from the ligand molecules on the spectrum. To isolate the effect of the NCs, measurements were also performed on the aerosol obtained by atomization of the "blank solution", containing only ligands dissolved in hexane. The resulting velocity map images, presented in Figure SI9, showed a clear difference in radius, between the two systems, indicating different IPs. The corresponding photoemission spectra extracted from the images are shown in Figure 2d. The ionization threshold of the particles produced by atomization of the NC organocolloid is distinct and obvious in Figure 2d, defining the valence band maximum of $MAPbBr_3$ NCs as 6.00 ± 0.05 eV. The threshold observed in the spectrum of the "blank solution" aerosol appears ∼1 eV below the measured IPs of single molecules (Figure 2c). This effect is due to clustering of the ligand molecules in the aerosol source, producing nanodroplets with IPs lower than the individual molecules (see Figure SI10). A shift of up to 1 eV is typically reported for such an effect.[16,32−34] Note that, to our best knowledge, photoelectron spectra of OA, either as a free molecule or in an aerosol, has never been investigated before.



DOI: 10.1021/acs.jpclett.8b01466
J. Phys. Chem. Lett. 2018, 9, 3604−3611

A synthesis of the experimental and theoretical results is given in Figure 3. Our study shows that the electronic structure of $MAPbBr_3$ NCs with a size range of 8−15 nm (commonly investigated previously) does not differ significantly from the bulk material. The calculated density of states (DOS) for $MAPbBr_3$ cubic perovskite bulk material, broadened by a Gaussian with a standard deviation of 0.3 eV, is shown on the left panel in Figure 3. However, it is important to point out that, in using the LARP method[10] to produce $MAPbBr_3$ NCs, the attached ligands may have a significant influence on the apparent valence properties of the resulting NCs. Although the IPs of OA and OL are shown to be above the NC VBM, size reduction increases the VBM, while at the same time, the increase concentration of ligands could lead to clustering that reduces their IPs, potentially making them indistinguishable. The calculated quantum confinement energy in the valence band of $MAPbBr_3$ cubic perovskite NCs, as a function of their diameter (Figure 3, right panel), shows a strong increase of the VBM for the NCs below 10 nm.

In conclusion, we have performed a detailed investigation of the electronic properties of $CH_3NH_3PbBr_3$ NCs using a range of complementary PES techniques, together with independent DFT calculations. For the first time, to our knowledge, we have probed isolated $MAPbBr_3$ perovskite NCs by XPS and VUV PES methods, allowing for direct band alignment with respect to the vacuum level and a detailed study of the attached ligand molecules. The latter do not seem to modify the structure or affect the intrinsic properties of the perovskite NC. However, the ligand molecules can affect the experimental characterization of the NCs and produce additional effects that can influence the properties of the material on the macroscopic level. Indeed, the presence of ligand molecules has recently been identified as one of the major issues in present application of LHP NCs in optoelectronic applications.[9,10] By combining gas-phase and surface XPS, we determined the work function for the crystals of about 11 nm, which was found to be very similar to that of bulk material. The present technique opens up new possibilities for precise and detailed investigation of the electronic properties of LHP NCs, as well as other similar materials and different capping molecules, and for a range of nanoparticle sizes. Such an approach can quickly provide complementary information for material development.

## EXPERIMENTAL AND THEORETICAL SECTION

*Sample Preparation and Characterization.* $MAPbBr_3$ NCs were synthesized by the emulsion synthesis method using a previously reported procedure,[27] which was scaled up to produce a sufficient amount of the colloidal solutions for the aerosol studies. Briefly, we dissolved 179.2 mg of $CH_3NH_3Br$ and 734.4 mg of $PbBr_2$ in 3 and 5 mL of DMF solution, respectively. Next we mixed these two precursor solutions and stirred for 10 min. To form the emulsion, the resulting solution was added dropwise to the mixture of hexane (100 mL), OA (5 mL for SNC and 2 mL for BNC), and OL (200 $\mu$L), 80 mL of tertiary butanol was added to this solution to start demulsion, and the precipitate was collected by centrifugation at 6000 rpm for 5 min. To form the colloidal solution, the precipitate was redissolved in 40 mL of hexane and centrifuged at 5000 rpm for 5 min. The green fluorescent supernatant containing $MAPbBr_3$ nanocrystals was collected and used in the experiments reported here.

The XRD pattern was acquired using a Bruker D8 Advanced Davinci powder X-ray diffractometer with a Cu-$K_\alpha$ ($\lambda$ = 1.5406 Å) source. TEM was carried out using an FEITecnaiF30 high-resolution transmission electron microscope operating at a 300 keV accelerating voltage. Dynamic light scattering (DLS) measurements were performed by using a Nanotrac ULTRA (Microtrac) instrument. The BNC were not examined by TEM; thus their crystal size has been estimated according to DLS measurements.

*Surface XPS.* High-resolution photoemission spectra were recorded using an XPS apparatus (SPECS Surface Nano Analysis GmbH). This apparatus was used previously to characterize surfaces of $CH_3NH_3PbI_3$ perovskite films.[35] A photon beam with an energy of 1486.7 eV was generated from an aluminum anode in a microfocus X-ray (XR-MF) source. The XR-MF source was also equipped with a quartz crystal mirror as a monochromator, producing the monochromatic Al-$K_\alpha$ X-ray beam. A PHOIBOS 150 hemispherical energy analyzer (HEA) with a nine-single-channel electron multiplier detector (MCD-9) was used to collect photoemission spectra. High-resolution spectra were recorded with a pass energy of 20 eV, which gave a full width at half-maximum (fwhm) of ∼0.5 eV for the Au $4f_{7/2}$ peak. We calibrated the BE of the photoemission spectra with reference to C 1s at 285.3 eV.[35]

*Gas-Phase XPS.* Formation of Aerosol Nanocrystals for XPS and VUV ARPES. $MAPbBr_3$ aerosols were generated by atomization of the organocolloid solution (with hexane as the solvent) using a TSI 3076 atomizer. The resulting aerosols were transported, using 2.5 bar of Ar carrier gas, first through a metallic tube (gently heated to a temperature of about 40 °C to help evaporate hexane) and then through a cold trap (cooled to 0 °C to remove excess hexane from the beam) to the aerodynamic lens system (ALS, placed inside of a differentially pumped stage) that focused the nanoparticle beam into the high-vacuum interaction chambers of the spectrometers.

PLEIADES Beamline. The experiment was performed using the Multi-Purpose Source Chamber (MPSC) connected to the C-branch of the PLEIADES beamline, as described previously.[36] Aerosols containing the NCs were introduced in MPSC through a 200 $\mu$m limiting orifice, followed by an ALS focusing the nanoparticle beam, which was then directed through a skimmer to the ionization chamber at a $10^{-8}$ mbar base pressure ($10^{-6}$−$10^{-5}$ mbar working pressure). The NC beam was crossed by the beam of monochromatized linearly polarized (in the present case) synchrotron radiation from the magnetic undulator. Both the exit of the ALS and the skimmer position can be remotely controlled to align the nanoparticle beam to the photon beam, which is monitored by a total photoelectron yield from the NCs measured by a channeltron. Gas-phase XPS spectra presented in this work were recorded using a ±30° aperture wide-angle lens VG-Scienta R4000 electron energy analyzer, at incident photon energies of 140 and 600 eV. A permanent magnet APPLE II type undulator, with a period of 80 mm, was used as the synchrotron radiation source, in combination with a high-flux 600 l/mm grating used to monochromatize the synchrotron radiation produced by the undulator. The exit slit of the modified Petersen plane grating monochromator was set to 200 $\mu$m for 600 eV and 400 $\mu$m for 140 eV photon energies, yielding an overall resolution in the XPS spectra of about 0.8 and 0.2 eV, respectively. The photon energy was calibrated, depending on the range, according to several different transitions: Ne (1s → 3p) at 867.14 eV,[37] $N_2$ (N 1s, v = 0 → $\pi^*$) at 400.865 eV,[38] and $SF_6$ (S 2 → $2t_g$) at 184.5 eV.[39] Calibration gases were introduced into the



DOI: 10.1021/acs.jpclett.8b01466
J. Phys. Chem. Lett. 2018, 9, 3604−3611

calibration chamber (downstream of the XPS measurements) by an effusive jet crossing at a right angle the SR beam where photoions were extracted by a continuous electric field to a multichannel plate chevron stack, which amplified the signal to be detected by pulse counting electronics. Calibrations were performed several times during the experiment, and the overall accuracy of the photon energy calibration was estimated to be 0.3 eV, not including the accuracy of the literature values used as reference points. Note that uncertainty in the photon energy does not influence calibration of the BE scale, which has been determined from the measured kinetic energies of the Auger lines and IPs of the Ar carrier gas. The linearity of the photoelectron kinetic energy scale has been calibrated according to the 3p, 3s, 2p, and 2s Ar IPs,[40,41] as well as the Ar $L_3M_{23}M_{23}$ Auger line.[42] The BE scale of the XPS spectra, with respect to vacuum (BEV), was then obtained according to the convoluted Ar 3p IP at 15.80 eV. The overall uncertainty of the BEV is estimated to be 0.2 eV.

DESIRS Beamline. VUV ARPES/PEPICO experiments were performed on the SAPHIRS endstation[43] of the undulator-based VUV beamline DESIRS.[44] The NC aerosols were passed through a 200 $\mu$m limiting orifice that ensured 6 mbar of pressure in the aerodynamic lens system (ALS) during the experiment. The focused aerosol beam (420 $\pm$ 50 $\mu$m in diameter in the interaction region) was skimmed twice before arriving at the ionization chamber at a $10^{-8}$ mbar base pressure. In the chamber, the aerosol beam was crossed by the beam of circularly polarized synchrotron radiation ($h\nu$ = 8−16 eV, flux = $10^{12}$−$10^{13}$ photons/s). The electrons and ions formed in the interaction region (420 × 100 × 100 $\mu$m volume) were detected and analyzed by the double-imaging photoelectron−photoion coincidence DELICIOUS III spectrophotometer,[45] which combines velocity map imaging (VMI) on the electron side (providing AR-PES) with a 3D momentum imaging/time-of-flight spectrometer for detecting the coincident gas-phase cations. The PES data on the NPs were treated by considering all of the electrons, while the PES data on free gas-phase species were obtained by considering only the electrons in coincidence with a given cation ($m/z$ selection). From the recorded velocity map images, the PES were calculated by using the image inversion pBasex algorithm.[46]

*Calculations.* Ionization Potential of Molecules in the Gas Phase. IPs of molecules in the gas phase were calculated by the definition as IP(M) = $E(M^+) - E(M)$, where $E(M^+)$ is the energy of the positive ion and $E(M)$ is the energy of the neutral molecule. These energies were calculated using DFT, where exchange−correlation energy was modeled using the B3LYP functional,[47−49] which was shown to yield accurate values of IPs for a variety of organic molecules.[31] Calculations were performed using the NWChem code,[50] and the 6-31G* basis set was used to represent the wave functions.

Density of States of Bulk $CH_3NH_3PbBr_3$. To understand the spectra obtained, we performed DFT calculations of the electronic structure of cubic bulk $CH_3NH_3PbBr_3$. The correlation term was modeled using the local density approximation, while the exchange term was modeled using the modified Becke−Johnson potential[51] using the parametrization of ref 52, which was shown to yield accurate band gaps of halide perovskite materials. Effects of spin−orbit interaction were also included. Calculations have been performed using the Abinit code.[53,54] Core electrons were treated using Hartwigsen−Goedecker−Hutter pseudopotentials,[49] while wave functions were represented using plane waves with a 50 Ha kinetic energy cutoff. A constant energy shift was applied to the calculated DOS to match the VBM energy with the experimental one. In figures presented, the DOS was also broadened by a Gaussian with a standard deviation of 0.3 eV.

Quantum Confinement Energy in the Valence Band of $CH_3NH_3PbBr_3$ Nanocrystals. The VBM of cubic $CH_3NH_3PbBr_3$ is located at the R point of the Brillouin zone. Consequently, the highest occupied states of $CH_3NH_3PbBr_3$ are derived from R point states of bulk $CH_3NH_3PbBr_3$. The dispersion of the cubic material around the VBM is isotropic, and we modeled it as parabolic dispersion with effective mass $m^*$. The quantum confinement energy was then calculated by solving the corresponding Schrödinger equation for a particle of mass $m^*$ in a sphere with infinite potential at the boundary of the sphere. The value of the effective mass was set to $m^* = 0.15m_0$ (where $m_0$ is the free electron mass), which is close to the values reported for an analogue inorganic material $CsPbBr_3$.[55,56] We note that calculation of the band structure of one unit cell of $CH_3NH_3PbBr_3$ does not yield an isotropic dispersion around the VBM due to the effect of organic group orientation, which sets a preferential direction. Dispersion in a real $CH_3NH_3PbBr_3$ material is on average isotropic due to different orientations of organic groups in different unit cells, which on average restore isotropy. Full calculation of the band dispersion that takes these effects into account is a rather challenging task and is beyond the scope of this work. For these reasons, we choose to approximate the valence band dispersion of $CH_3NH_3PbBr_3$ with the valence band dispersion of the corresponding inorganic cubic $CsPbBr_3$, whose valence band dispersion around the R point is fully isotropic.

## ■ ASSOCIATED CONTENT

### Supporting Information

The Supporting Information is available free of charge on the ACS Publications website at DOI: 10.1021/acs.jpclett.8b01466.

Preparation procedure for $CH_3NH_3PbBr_3$ nanocrystals, transmission electron microscopy images of nanocrystals, XRD pattern, UV−vis absorption spectrum, supplementary gas-phase photoelectron spectra both in two-dimensions and as integrated spectra, mass spectra from VUV PEPICO measurements, velocity map images, and calculated density of electronic states of bulk $CH_3NH_3PbBr_3$ (PDF)

## ■ AUTHOR INFORMATION


### Corresponding Author

*E-mail: milosavljevic@synchrotron-soleil.fr.

### ORCID

Aleksandar R. Milosavljević: 0000-0003-3541-8872
Dušan K. Božanić: 0000-0001-8246-9635
Nenad Vukmirović: 0000-0002-4101-1713
Weixin Huang: 0000-0003-1456-4387
Sylwia Ptasinska: 0000-0002-7550-8189

### Present Addresses

#S.S.: Université Bordeaux CNRS UMR 5255, ISM, F-33405 Talence, France.




DOI: 10.1021/acs.jpclett.8b01466
J. Phys. Chem. Lett. 2018, 9, 3604−3611

[▽]R.D.: Department of Chemistry and Biochemistry, University of Notre Dame, 251 Nieuwland Science Hall, Notre Dame, Indiana 46556, U.S.A.

### Notes

The authors declare no competing financial interest.

## ■ ACKNOWLEDGMENTS

S.S., P.S., W.H., and S.P. acknowledge the U.S. Department of Energy Office of Science, Office of Basic Energy Sciences under Award Number DE-FC02-04ER15533 (NDRL no: 5205). N.V. and R.D. acknowledge support from the Ministry of Education, Science and Technological Development of the Republic of Serbia (Projects ON171017; OI172056 and III45020, respectively). N.V. also acknowledges support from the European Commission under H2020 project VI-SEEM, Grant No. 675121. Numerical computations were performed on the PARADOX supercomputing facility at the Scientific Computing Laboratory of the Institute of Physics Belgrade. The SOLEIL synchrotron radiation facility is acknowledged for providing beamtime under Projects 20170609 and 20160324.

## ■ REFERENCES

(1) Kojima, A.; Teshima, K.; Shirai, Y.; Miyasaka, T. Organometal Halide Perovskites as Visible-Light Sensitizers for Photovoltaic Cells. *J. Am. Chem. Soc.* **2009**, *131* (17), 6050−6051.

(2) Lee, M. M.; Teuscher, J.; Miyasaka, T.; Murakami, T. N.; Snaith, H. J. Efficient Hybrid Solar Cells Based on Meso-Superstructured Organometal Halide Perovskites. *Science* **2012**, *338* (6107), 643−647.

(3) Snaith, H. J. Perovskites: The Emergence of a New Era for Low-Cost, High-Efficiency Solar Cells. *J. Phys. Chem. Lett.* **2013**, *4*, 3623−3630.

(4) Zhou, H.; Chen, Q.; LI, G.; Luo, S.; Song, T.-b.; et al. Interface Engineering of Highly Efficient Perovskite Solar Cells. *Science (Washington, DC, U. S.)* **2014**, *345* (6196), 542−546.

(5) Jeon, N. J.; Noh, J. H.; Kim, Y. C.; Yang, W. S.; Ryu, S.; Seok, S. I. Solvent Engineering for High-Performance Inorganic-Organic Hybrid Perovskite Solar Cells. *Nat. Mater.* **2014**, *13*, 897−903.

(6) Jeon, N. J.; Noh, J. H.; Yang, W. S.; Kim, Y. C.; Ryu, S.; Seo, J.; Seok, S. Il. Compositional Engineering of Perovskite Materials for High-Performance Solar Cells. *Nature* **2015**, *517* (7535), 476−480.

(7) Chen, Q.; De Marco, N.; Yang, Y.; Song, T.-B.; Chen, C.-C.; Zhao, H.; Hong, Z.; Zhou, H.; Yang, Y. Under the Spotlight: The Organic−inorganic Hybrid Halide Perovskite for Optoelectronic Applications. *Nano Today* **2015**, *10* (3), 355−396.

(8) Kovalenko, M. V.; Protesescu, L.; Bodnarchuk, M. I. Properties and Potential Optoelectronic Applications of Lead Halide Perovskite Nanocrystals. *Science (Washington, DC, U. S.)* **2017**, *358*, 745−750.

(9) Akkerman, Q. A.; Rainò, G.; Kovalenko, M. V.; Manna, L. Genesis, Challenges and Opportunities for Colloidal Lead Halide Perovskite Nanocrystals. *Nat. Mater.* **2018**, *17*, 394−405.

(10) Hong, K.; Le, Q. V.; Kim, S. Y.; Jang, H. W. Low-Dimensional Halide Perovskites: Review and Issues. *J. Mater. Chem. C* **2018**, *6*, 2189−2209.

(11) Endres, J.; Egger, D. A.; Kulbak, M.; Kerner, R. A.; Zhao, L.; Silver, S. H.; Hodes, G.; Rand, B. P.; Cahen, D.; Kronik, L.; et al. Valence and Conduction Band Densities of States of Metal Halide Perovskites: A Combined Experimental-Theoretical Study. *J. Phys. Chem. Lett.* **2016**, *7* (14), 2722−2729.

(12) Butler, K. T.; Frost, J. M.; Walsh, A. Band Alignment of the Hybrid Halide Perovskites $CH_3NH_3PbCl_3$, $CH_3NH_3PbBr_3$ and $CH_3NH_3PbI_3$. *Mater. Horiz.* **2015**, *2* (2), 228−231.

(13) Philippe, B.; Jacobsson, T. J.; Correa-Baena, J. P.; Jena, N. K.; Banerjee, A.; Chakraborty, S.; Cappel, U. B.; Ahuja, R.; Hagfeldt, A.; Odelius, M.; et al. Valence Level Character in a Mixed Perovskite Material and Determination of the Valence Band Maximum from Photoelectron Spectroscopy: Variation with Photon Energy. *J. Phys. Chem. C* **2017**, *121* (48), 26655−26666.

(14) Axnanda, S.; Scheele, M.; Crumlin, E.; Mao, B.; Chang, R.; Rani, S.; Faiz, M.; Wang, S.; Alivisatos, A. P.; Liu, Z. Direct Work Function Measurement by Gas Phase Photoelectron Spectroscopy and Its Application on PbS Nanoparticles. *Nano Lett.* **2013**, *13* (12), 6176−6182.

(15) Sublemontier, O.; Nicolas, C.; Aureau, D.; Patanen, M.; Kintz, H.; Liu, X.; Gaveau, M.-A.; Le Garrec, J.-L.; Robert, E.; Barreda, F.-A.; et al. X-Ray Photoelectron Spectroscopy of Isolated Nanoparticles. *J. Phys. Chem. Lett.* **2014**, *5* (19), 3399−3403.

(16) Gaie-Levrel, F.; Garcia, G. a.; Schwell, M.; Nahon, L. VUV State-Selected Photoionization of Thermally-Desorbed Biomolecules by Coupling an Aerosol Source to an Imaging Photoelectron/photoion Coincidence Spectrometer: Case of the Amino Acids Tryptophan and Phenylalanine. *Phys. Chem. Chem. Phys.* **2011**, *13* (15), 7024−7036.

(17) Xiong, W.; Hickstein, D. D.; Schnitzenbaumer, K. J.; Ellis, J. L.; Palm, B. B.; Keister, K. E.; Ding, C.; Miaja-avila, L.; Dukovic, G.; Jimenez, J. L.; et al. Photoelectron Spectroscopy of CdSe Nanocrystals in the Gas Phase : A Direct Measure of the Evanescent Electron Wave Function of Quantum Dots. *Nano Lett.* **2013**, *13*, 2924−2930.

(18) Lindblad, R.; Jena, N. K.; Philippe, B.; Oscarsson, J.; Bi, D.; Lindblad, A.; Mandal, S.; Pal, B.; Sarma, D. D.; Karis, O.; et al. Electronic Structure of CH3NH3PbX3 Perovskites: Dependence on the Halide Moiety. *J. Phys. Chem. C* **2015**, *119* (4), 1818−1825.

(19) Zhang, Z.; Long, R.; Tokina, M. V.; Prezhdo, O. V. Interplay between Localized and Free Charge Carriers Can Explain Hot Fluorescence in the CH3NH3PbBr3Perovskite: Time-Domain Ab Initio Analysis. *J. Am. Chem. Soc.* **2017**, *139* (48), 17327−17333.

(20) Wenger, B.; Nayak, P. K.; Wen, X.; Kesava, S. V.; Noel, N. K.; Snaith, H. J. Consolidation of the Optoelectronic Properties of CH3NH3PbBr3 Perovskite Single Crystals. *Nat. Commun.* **2017**, *8* (1), 590.

(21) Sichert, J. a.; Tong, Y.; Mutz, N.; Vollmer, M.; Fischer, S.; Milowska, K. Z.; García Cortadella, R.; Nickel, B.; Cardenas-Daw, C.; Stolarczyk, J. K.; et al. Quantum Size Effect in Organometal Halide Perovskite Nanoplatelets. *Nano Lett.* **2015**, *15* (10), 6521−6527.

(22) Zhu, Q.; Zheng, K.; Abdellah, M.; Generalov, A.; Haase, D.; Carlson, S.; Niu, Y.; Heimdal, J.; Engdahl, A.; Messing, M. E.; et al. Correlating Structure and Electronic Band-Edge Properties in Organolead Halide Perovskites Nanoparticles. *Phys. Chem. Chem. Phys.* **2016**, *18*, 14933−14940.

(23) Zheng, K.; Abdellah, M.; Zhu, Q.; Kong, Q.; Jennings, G.; Kurtz, C. A.; Messing, M. E.; Niu, Y.; Gosztola, D. J.; Al-Marri, M. J.; et al. Direct Experimental Evidence for Photoinduced Strong-Coupling Polarons in Organolead Halide Perovskite Nanoparticles. *J. Phys. Chem. Lett.* **2016**, *7* (22), 4535−4539.

(24) Telfah, H.; Jamhawi, A.; Teunis, M. B.; Sardar, R.; Liu, J. Ultrafast Exciton Dynamics in Shape-Controlled Methylammonium Lead Bromide Perovskite Nanostructures: Effect of Quantum Confinement on Charge Carrier Recombination. *J. Phys. Chem. C* **2017**, *121* (51), 28556−28565.

(25) Gonzalez-Carrero, S.; Schmidt, L. C.; Rosa-Pardo, I.; Martínez-Sarti, L.; Sessolo, M.; Galian, R. E.; Pérez-Prieto, J. Colloids of Naked $CH_3NH_3PbBr_3$ Perovskite Nanoparticles: Synthesis, Stability, and Thin Solid Film Deposition. *ACS Omega* **2018**, *3* (1), 1298−1303.

(26) Fu, X.; Peng, Z.; Zhang, C.; Xia, Y.; Zhang, J.; Luo, W.; Guo, L. J.; Li, H.; Wang, Y.; Zhang, D. Controlled Synthesis of Brightly Fluorescent CH3NH3PbBr3 Perovskite Nanocrystals Employing Pb(C17H33COO)2 as the Sole Lead Source. *RSC Adv.* **2018**, *8*, 1132−1139.

(27) Huang, H.; Zhao, F.; Liu, L.; Zhang, F.; Wu, X. G.; Shi, L.; Zou, B.; Pei, Q.; Zhong, H. Emulsion Synthesis of Size-Tunable CH3NH3PbBr3Quantum Dots: An Alternative Route toward Efficient Light-Emitting Diodes. *ACS Appl. Mater. Interfaces* **2015**, *7* (51), 28128−28133.

(28) Mali, S. S.; Shim, C. S.; Hong, C. K. Highly Stable and Efficient Solid-State Solar Cells Based on Methylammonium Lead Bromide



DOI: 10.1021/acs.jpclett.8b01466
J. Phys. Chem. Lett. 2018, 9, 3604−3611

(CH3NH3PbBr3) Perovskite Quantum Dots. *NPG Asia Mater.* **2015**, *7* (8), e208−9.
(29) Olthof, S. Research Update: The Electronic Structure of Hybrid Perovskite Layers and Their Energetic Alignment in Devices. *APL Mater.* **2016**, *4*, 091502.
(30) Kahn, A. Fermi Level, Work Function and Vacuum Level. *Mater. Horiz.* **2016**, *3*, 7.
(31) Zhan, C.-G.; Nichols, J. A.; Dixon, D. A. Ionization Potential, Electron Affinity, Electronegativity, Hardness, and Electron Excitation Energy: Molecular Properties from Density Functional Theory Orbital Energies. *J. Phys. Chem. A* **2003**, *107* (20), 4184−4195.
(32) Brutschy, B.; Bisling, P.; Ruhl, E.; Baumgartel, H. Photoionization Mass Spectrometry of Molecular Clusters Using Synchrotron Radiation. *Z. Phys. D: At., Mol. Clusters* **1987**, *5*, 217−231.
(33) Barth, S.; Ončák, M.; Ulrich, V.; Mucke, M.; Lischke, T.; Slavíček, P.; Hergenhahn, U. Valence Ionization of Water Clusters: From Isolated Molecules to Bulk. *J. Phys. Chem. A* **2009**, *113* (48), 13519−13527.
(34) Joblin, C.; Dontot, L.; Garcia, G. A.; Spiegelman, F.; Rapacioli, M.; Nahon, L.; Parneix, P.; Pino, T.; Bréchignac, P. Size Effect in the Ionization Energy of PAH Clusters. *J. Phys. Chem. Lett.* **2017**, *8* (15), 3697−3702.
(35) Milosavljevic, A. R.; Huang, W.; Sadhu, S.; Ptasinska, S. Low-Energy Electron-Induced Transformations in Organolead Halide Perovskite. *Angew. Chem., Int. Ed.* **2016**, *55* (34), 10083−10087.
(36) Lindblad, A.; Söderström, J.; Nicolas, C.; Robert, E.; Miron, C. A Multi Purpose Source Chamber at the PLEIADES Beamline at SOLEIL for Spectroscopic Studies of Isolated Species: Cold Molecules, Clusters, and Nanoparticles. *Rev. Sci. Instrum.* **2013**, *84* (11), 113105.
(37) Coreno, M.; Avaldi, L.; Camilloni, R.; Prince, K. C.; de Simone, M.; Karvonen, J.; Colle, R.; Simonucci, S. Measurement and Ab Initio Calculation of the Ne Photoabsorption Spectrum in the Region of the K Edge. *Phys. Rev. A: At., Mol., Opt. Phys.* **1999**, *59* (3), 2494−2497.
(38) Kato, M.; Morishita, Y.; Oura, M.; Yamaoka, H.; Tamenori, Y.; Okada, K.; Matsudo, T.; Gejo, T.; Suzuki, I. H.; Saito, N. Absolute Photoionization Cross Sections with Ultra-High Energy Resolution for Ar, Kr, Xe and N 2 in Inner-Shell Ionization Regions. *J. Electron Spectrosc. Relat. Phenom.* **2007**, *160*, 39−48.
(39) Sze, K. H.; Brion, C. E. Inner-Shell and Valence-Shell Electronic Excitation of SFs, $SeF_6$ and TeFa by High Energy Electron Impact: An Investigation of Potential Barrier Effects. *Chem. Phys.* **1990**, *140*, 439−472.
(40) Svensson, S.; Eriksson, B.; Martensson, N.; Gelius, U.; Wendin, G. Electron Shake-up and Correlation Satellites and Continuum Shake-off Distributions in X-ray Photoelectron Spectra of the Rare Gas Atoms. *J. Electron Spectrosc. Relat. Phenom.* **1988**, *47*, 327−384.
(41) Thompson. *X-ray Data Booklet*; 2001.
(42) Werme, L.; Bergmark, T.; Siegbahn, K. The L 2,3 MM Auger Spectrum of Argon. *Phys. Scr.* **1973**, *8*, 149−158.
(43) Tang, X.; Garcia, G. A.; Gil, J.; Nahon, L. Vacuum Upgrade and Enhanced Performances of the Double Imaging Electron/ion Coincidence End-Station at the Vacuum Ultraviolet Beamline DESIRS. *Rev. Sci. Instrum.* **2015**, *86*, 123108.
(44) Nahon, L.; de Oliveira, N.; Garcia, G. a.; Gil, J.-F.; Pilette, B.; Marcouillé, O.; Lagarde, B.; Polack, F. DESIRS: A State-of-the-Art VUV Beamline Featuring High Resolution and Variable Polarization for Spectroscopy and Dichroism at SOLEIL. *J. Synchrotron Radiat.* **2012**, *19*, 508−520.
(45) Garcia, G. A.; Cunha de Miranda, B. K.; Tia, M.; Daly, S.; Nahon, L. DELICIOUS III: A Multipurpose Double Imaging Particle Coincidence Spectrometer for Gas Phase Vacuum Ultraviolet Photodynamics Studies. *Rev. Sci. Instrum.* **2013**, *84*, 053112.
(46) Garcia, G. A.; Nahon, L.; Powis, I. Two-Dimensional Charged Particle Image Inversion Using a Polar Basis Function Expansion. *Rev. Sci. Instrum.* **2004**, *75* (11), 4989−4996.
(47) Becke, A. D. Density-Functional Thermochemistry. III. The Role of Exact Exchange. *J. Chem. Phys.* **1993**, *98* (7), 5648−5652.
(48) Stephens, P. J.; Devlin, F. J.; Chabalowski, C. F.; Frisch, M. J. Ab Initio Calculation of Vibrational Absorption and Circular Dichroism Spectra Using Density Functional Force Fields. *J. Phys. Chem.* **1994**, *98* (45), 11623−11627.
(49) Hartwigsen, C.; Goedecker, S.; Hutter, J. Relativistic Separable Dual-Space Gaussian Pseudopotentials from H to Rn. *Phys. Rev. B: Condens. Matter Mater. Phys.* **1998**, *58* (7), 3641−3662.
(50) Valiev, M.; Bylaska, E. J.; Govind, N.; Kowalski, K.; Straatsma, T. P.; Van Dam, H. J. J.; Wang, D.; Nieplocha, J.; Apra, E.; Windus, T. L.; et al. NWChem: A Comprehensive and Scalable Open-Source Solution for Large Scale Molecular Simulations. *Comput. Phys. Commun.* **2010**, *181* (9), 1477−1489.
(51) Tran, F.; Blaha, P. Accurate Band Gaps of Semiconductors and Insulators with a Semilocal Exchange-Correlation Potential. *Phys. Rev. Lett.* **2009**, *102* (22), 5−8.
(52) Jishi, R. A.; Ta, O. B.; Sharif, A. A. Modeling of Lead Halide Perovskites for Photovoltaic Applications. *J. Phys. Chem. C* **2014**, *118* (49), 28344−28349.
(53) Gonze, X.; Jollet, F.; Abreu Araujo, F.; Adams, D.; Amadon, B.; Applencourt, T.; Audouze, C.; Beuken, J. M.; Bieder, J.; Bokhanchuk, A.; et al. Recent Developments in the ABINIT Software Package. *Comput. Phys. Commun.* **2016**, *205*, 106−131.
(54) Marques, M. A. L.; Oliveira, M. J. T.; Burnus, T. Libxc: A Library of Exchange and Correlation Functionals for Density Functional Theory. *Comput. Phys. Commun.* **2012**, *183* (10), 2272−2281.
(55) Protesescu, L.; Yakunin, S.; Bodnarchuk, M. I.; Krieg, F.; Caputo, R.; Hendon, C. H.; Yang, R. X.; Walsh, A.; Kovalenko, M. V. Nanocrystals of Cesium Lead Halide Perovskites (CsPbX3, X = Cl, Br, and I): Novel Optoelectronic Materials Showing Bright Emission with Wide Color Gamut. *Nano Lett.* **2015**, *15* (6), 3692−3696.
(56) Becker, M. A.; Vaxenburg, R.; Nedelcu, G.; Sercel, P. C.; Shabaev, A.; Mehl, M. J.; Michopoulos, J. G.; Lambrakos, S. G.; Bernstein, N.; Lyons, J. L.; et al. Bright Triplet Excitons in Caesium Lead Halide Perovskites. *Nature* **2018**, *553* (7687), 189−193.


DOI: 10.1021/acs.jpclett.8b01466
*J. Phys. Chem. Lett.* 2018, 9, 3604−3611

Supporting Information

# Electronic Properties of Free-Standing Surfactant-Capped Lead Halide Perovskite Nanocrystals Isolated *in Vacuo*

Aleksandar R. Milosavljević[1,*], Dušan K. Božanić[1,2], Subha Sadhu[3,a], Nenad Vukmirović[4], Radovan Dojčilović[2,b], Pitambar Sapkota[3,5], Weixin Huang[3], John Bozek[1], Christophe Nicolas[1], Laurent Nahon[1] and Sylwia Ptasinska[3,5]

[1]*Synchrotron SOLEIL, l'Orme des Merisiers, St Aubin, BP48, 91192 Gif sur Yvette Cedex, France.*

[2]*Vinča Institute of Nuclear Sciences, University of Belgrade, P.O. Box 522, 11001 Belgrade, Serbia*

[3]*Radiation Laboratory, University of Notre Dame, Notre Dame, IN 46556, USA.*

[4]*Scientific Computing Laboratory, Center for the Study of Complex Systems, Institute of Physics Belgrade, University of Belgrade, Pregrevica 118, 11080 Belgrade, Serbia.*

[5]*Department of Physics, University of Notre Dame, Notre Dame, IN 46556, USA.*

[*] Corresponding Authors: milosavljevic@synchrotron-soleil.fr (A.M.);

a: present address – Université Bordeaux CNRS UMR 5255, ISM, F-33405 Talence, France

b: present address – Department of Chemistry and Biochemistry, University of Notre Dame, 251 Nieuwland Science Hall, Notre Dame, Indiana 46556, USA

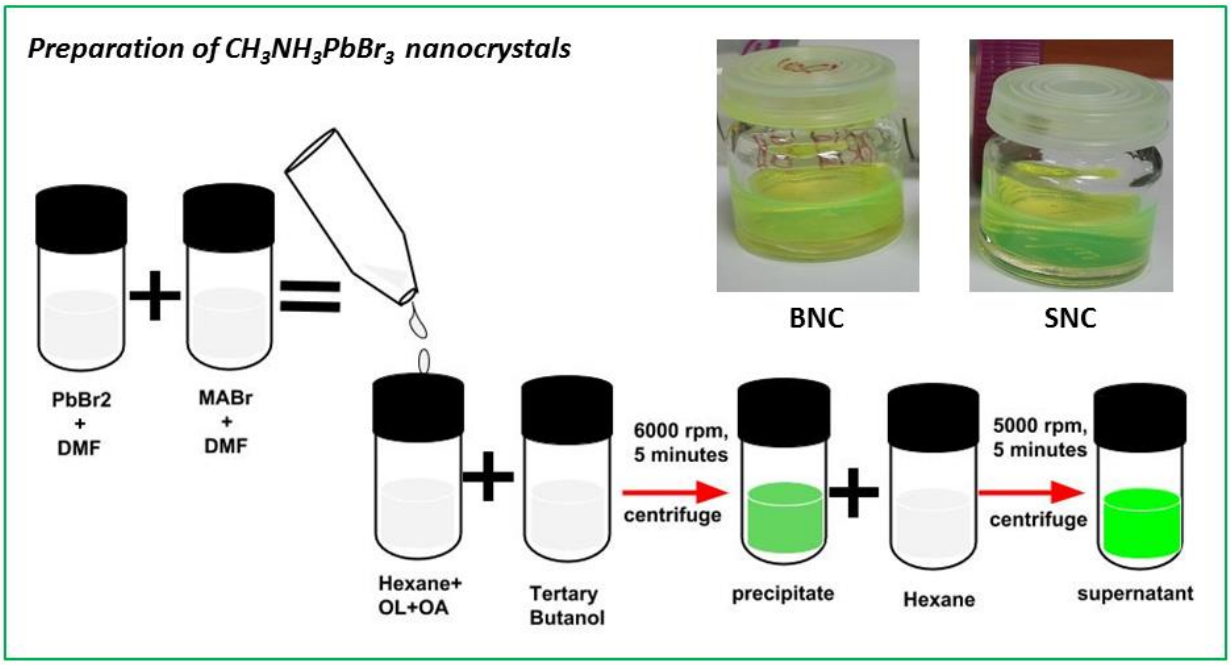


Figure SI1. A scheme of the preparation procedure for $CH_3NH_3PbBr_3$ nanocrystals. The insets show photos of the final solutions used in the atomizer to obtain the nanoparticle beam; SNC stands for small nanocrystals (~11 nm), BNC stands for big nanocrystals (~20 nm).

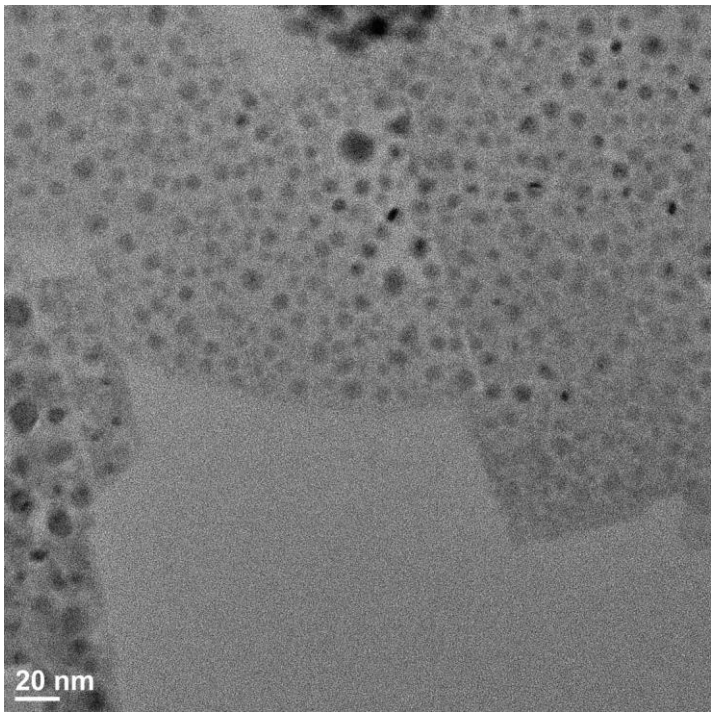


Figure SI2. Transmission electron microscopy images of $MAPbBr_3$ nanocrystals (SNC, as in Figure SI1).

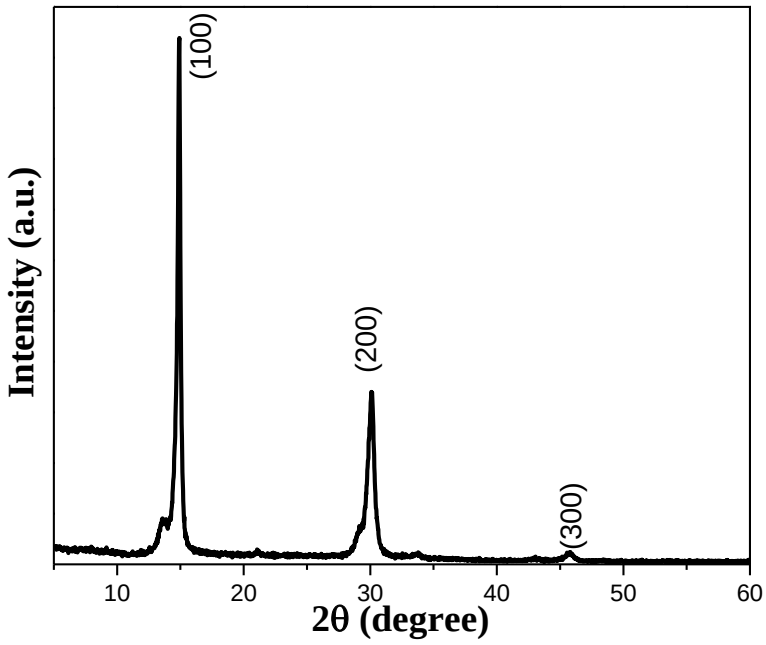


Figure SI3. X-ray diffraction (XRD) pattern of $MAPbBr_3$ nanocrystals (SNC, as in Figure SI1).

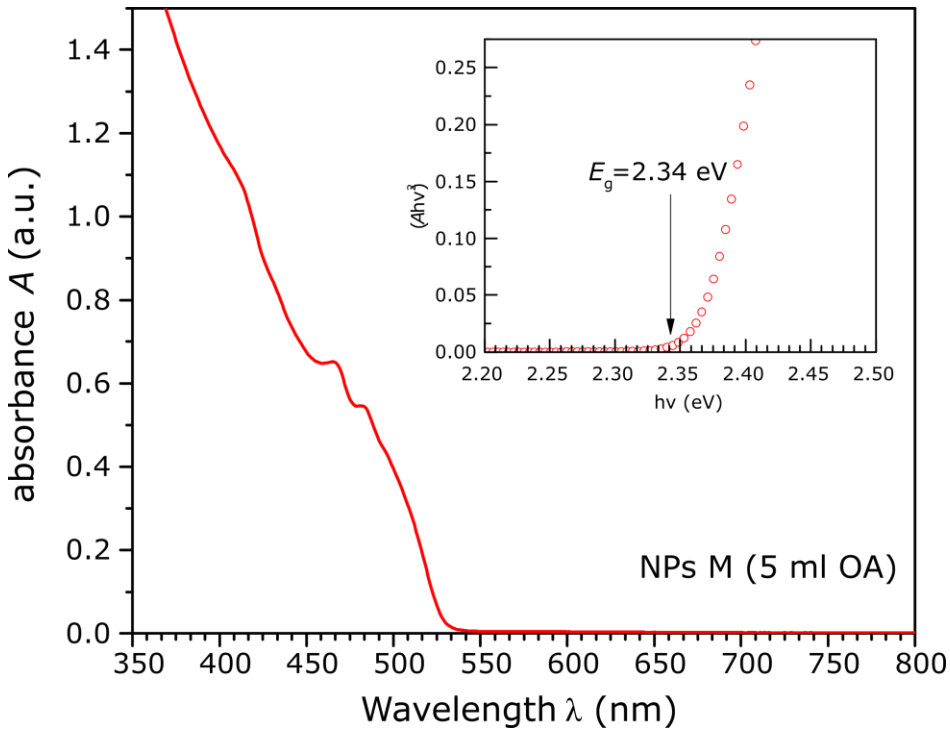


Figure SI4. UV-VIS absorption spectrum of $MAPbBr_3$ nanocrystal organocolloid (11±3 nm particle size) measured using Thermo Scientific Carry 4000 spectrophotometer.

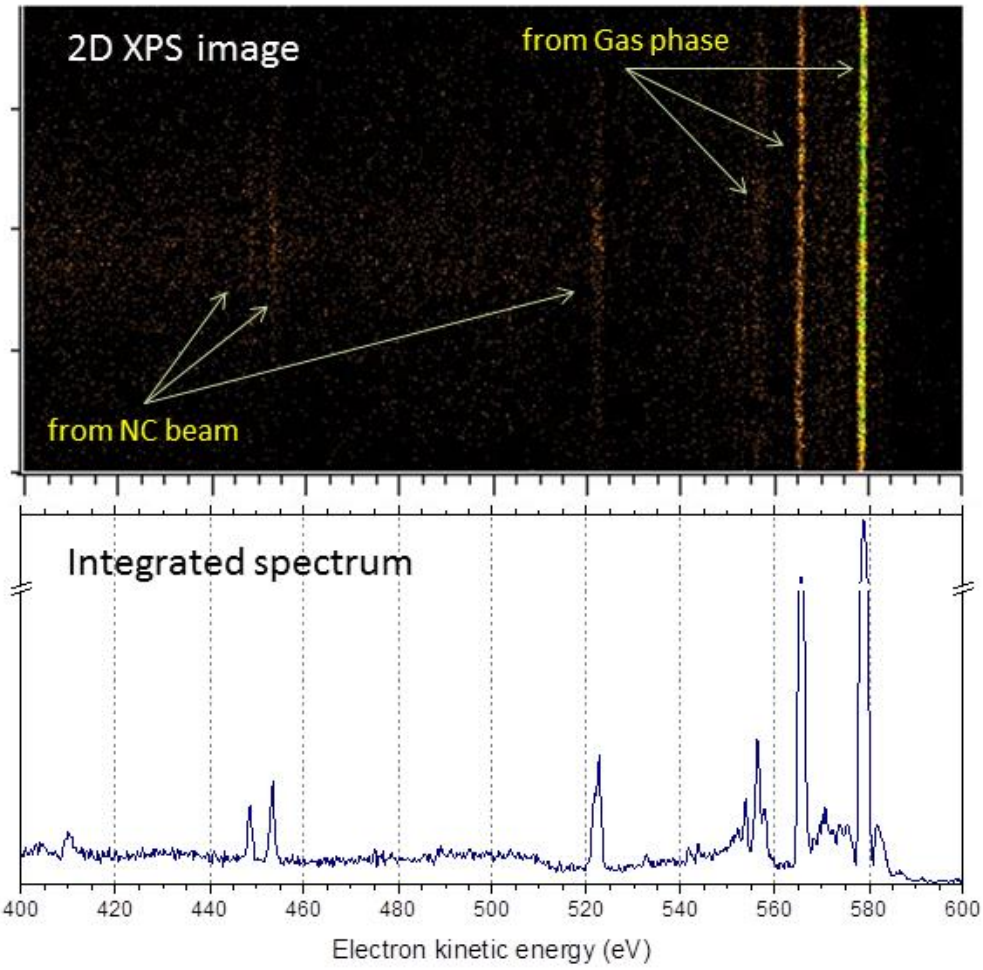


Figure SI5. Gas-phase XPS photoelectron spectrum in two-dimensions (top) and as an integrated spectrum (bottom). The kinetic energy distribution is obtained using a Scienta hemispherical analyzer, in transmission mode (all electrons emitted along the axis of the ionizing photon beam are focused to the same vertical position of the detector, independently from their emission angles), which images photoelectrons produced within a limited area defined roughly by the entrance slit, and disperses them according to their kinetic energies in the horizontal direction onto a position sensitive detector (top panel). The kinetic energy distribution (bottom panel) is then obtained by integrating the obtained 2D image along vertical lines. The axis of the electron energy dispersion coincides with the axis of the nanoparticle beam. Electrons from the central part of the beam are imaged onto the central (vertical) part of the 2D image (top panel). The large nanoparticles (c.a. 50-500 nm) are focused by the aerodynamic lenses to form a beam of a few hundred microns diameter, much smaller than the Scienta imaging area. The carrier Ar gas and small solvent molecules (hexane in the present case) are not focused by the aerodynamic lenses and form a diffuse cloud around the central nanoparticle beam and thus fill the whole vertical area of the detector. Therefore, photoelectron lines corresponding to the nanoparticle beam ("nano-phase") are seen in the center of the image while those from the gaseous non-focused species ("gas-phase") fill the whole image, allowing the two components to be easily identified. Note also that the background is dominantly produced from dense nanoparticle beam.

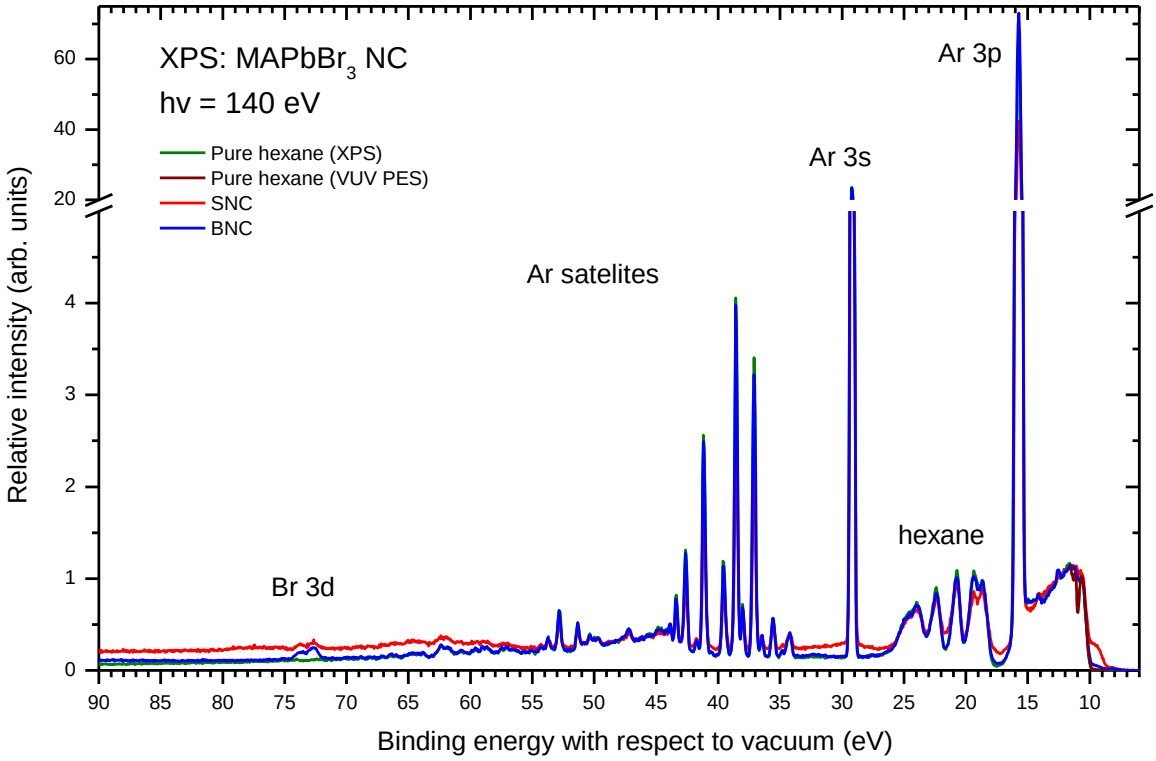


Figure SI6. Gas phase XPS of isolated MAPbBr nanocrystals of 11±3 nm (red line) and 20 nm (blue line), as well as pure hexane solution (green line) recorded at the PLEIADES beamline at the photon energy of 140 eV. The dark red line represents the VUV PEPICO spectrum of the pure hexane sample recorded at the DESIRS beamline.

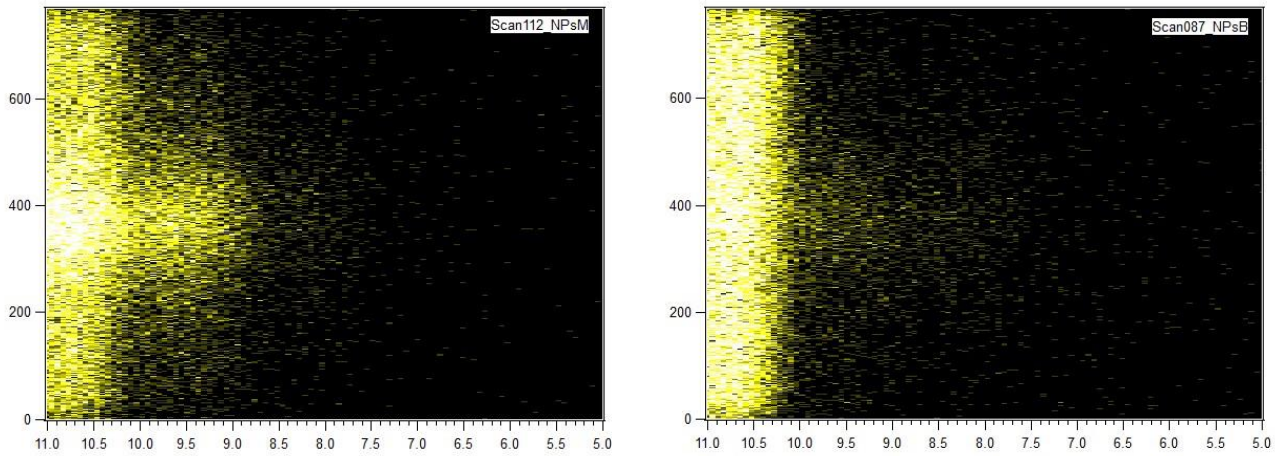


Figure SI7. 2D XPS images (see Figure SI5 for explanation) that correspond to the valence region of the XPS spectrum presented in Figure SI6 above, for SNC (left panel) and BNC (right panel). In both cases, the lower energy valence edges corresponding to nanocrystals and ligand molecules (OA and OL) are clearly restricted to the central part of the image, in contrast to the hexane valence edge (at about 10 eV) that is spread over the whole 2D image. Therefore, the photoelectrons from the ligand molecules OA and OL dominantly come from the focused nanoparticle beam, confirming that the probed ligands are attached to the nanocrystals. Note also that intensity from the ligands is much stronger for the case of the smaller nanocrystals, as discussed in the manuscript.

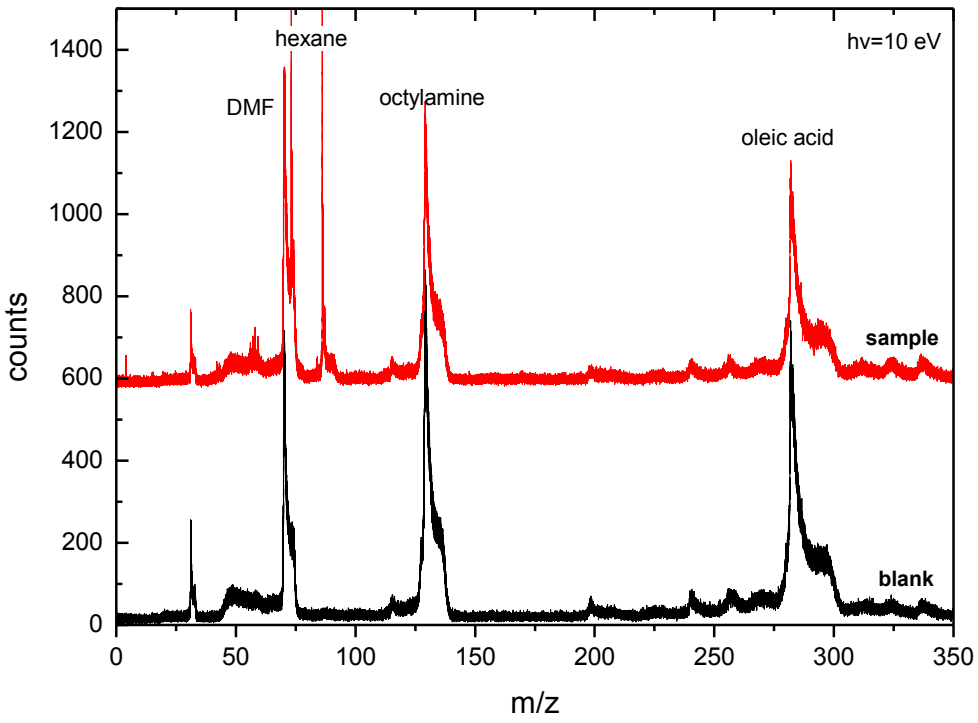


Figure SI8. The mass spectra of the $MAPbBr_3$ nanocrystal hexane dispersion (labeled 'sample') and the octylamine an oleic acids hexane solution ('blank') obtained at 10 eV photon energy. The spectra suggest presence of free surfactant molecules in the organocolloid. The contribution of the free molecules was subtracted from the net photoemission to obtain the PES of the $MAPbBr_3$ nanocrystals.

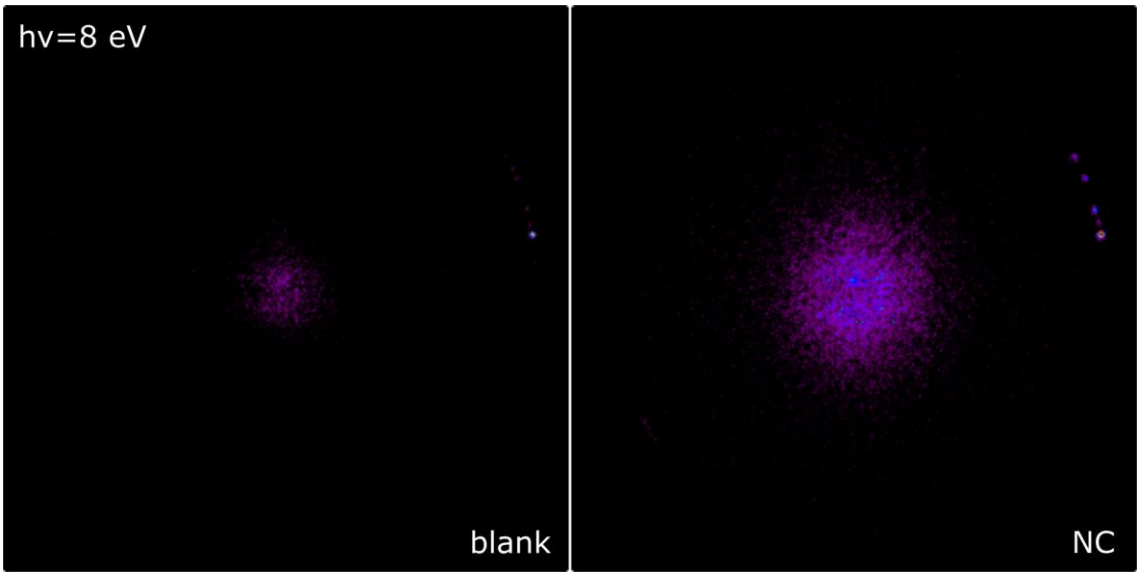


Figure SI9. The background-corrected velocity map images of the photoelectrons recorded for the blank solution (hexane+OA+OL) and the $MAPbBr_3$ NC sample at 8 eV photon energy.

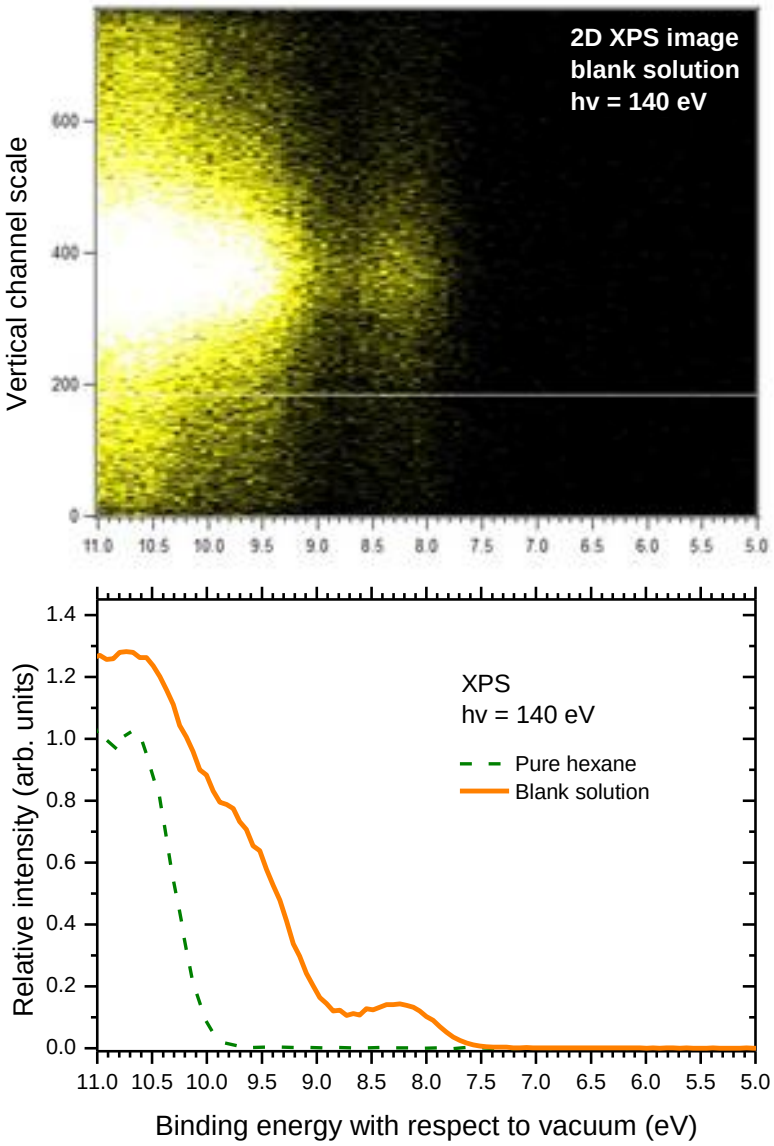


Figure SI10. 2D gas phase XPS images (top panel - see Figure SI5 for explanation) corresponding to the valence region of the XPS spectrum recorded at hv =140 eV for the "blank solution", containing only OA and OL molecules in hexane. The integrated spectrum is presented in the bottom panel (orange line). The XPS of pure hexane taken at the same photon energy is also presented for comparison (green dashed line). The 2D image indicates clustering of OA and OL molecules in the beam with a wide range of cluster sizes as evidenced by the increased intensity on axis for the red-shifted lower binding energies.

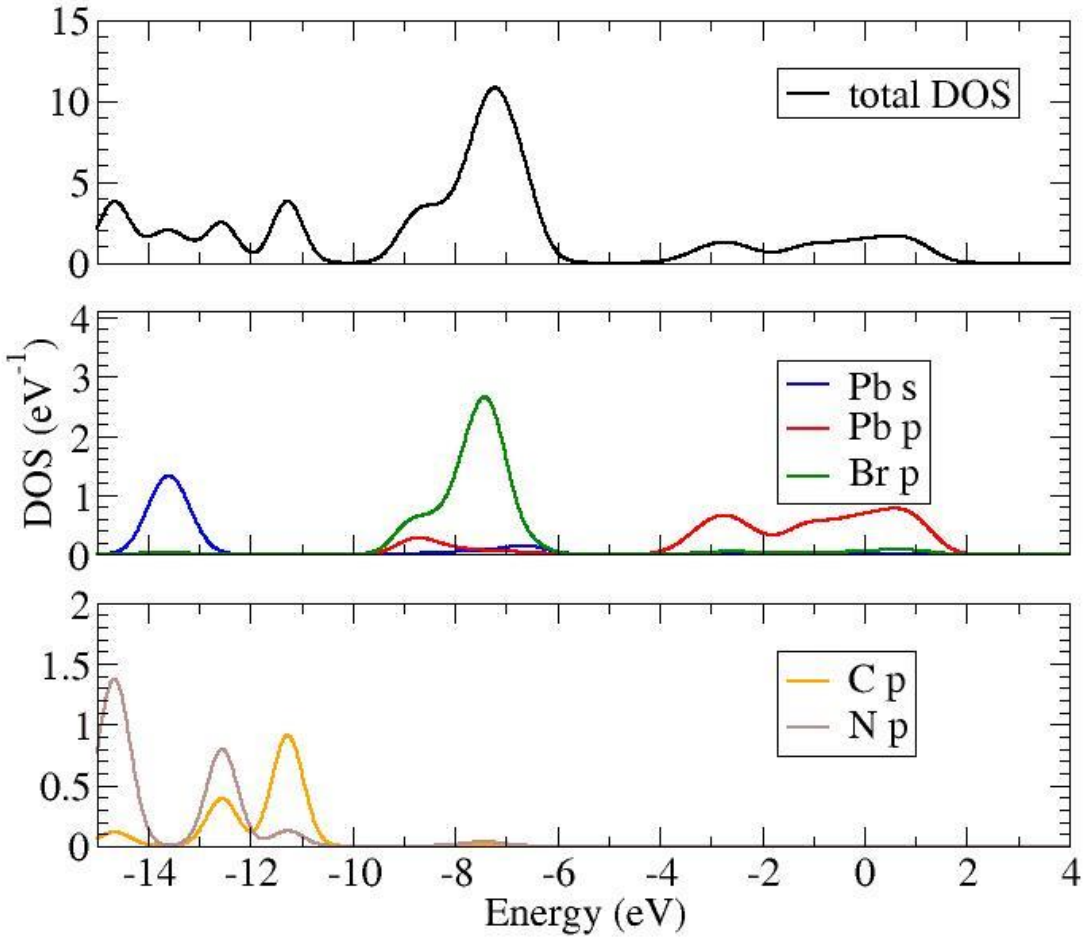


Figure SI11. Density of electronic states of bulk $CH_3NH_3PbBr_3$ obtained from density functional theory calculations. Total density of states is presented in the upper panel. Lower two panels present angular momentum projected partial density of states in the sphere surrounding an atom. The radius of the sphere was 1.4 bohr for C and N, 2.6 bohr for Pb, and 2.1 bohr for Br.